JOURNAL OF APPLIED CRYSTALLOGRAPHY

ISSN: 1600-5767
journals.iucr.org/j

X-ray asterism and the structure of cracks from indentations in silicon

B. K. Tanner, J. Garagorri, E. Gorostegui-Colinas, M. R. Elizalde, D. Allen, P. J. McNally, J. Wittge, C. Ehlers and A. N. Danilewsky

J. Appl. Cryst. (2016). **49**, 250–259

JOURNAL OF APPLIED CRYSTALLOGRAPHY

ISSN 1600-5767

X-ray asterism and the structure of cracks from indentations in silicon

B. K. Tanner,[a]* J. Garagorri,[b] E. Gorostegui-Colinas,[b]‡ M. R. Elizalde,[b] D. Allen,[c] P. J. McNally,[c] J. Wittge,[d]§ C. Ehlers[d]¶ and A. N. Danilewsky[d]

[a]Department of Physics, Durham University, South Road, Durham DH1 3LE, UK, [b]CEIT and Tecnun (University of Navarra), Paseo de Manuel Lardizabal 15, 20018 San Sebastián, Spain, [c]School of Electronic Engineering, Dublin City University, Dublin 9, Ireland, and [d]Kristallographie, Institut für Geo- und Umweltnaturwissenschaften, University of Freiburg, Freiburg, Germany. *Correspondence e-mail: b.k.tanner@dur.ac.uk

Received 9 September 2015
Accepted 22 December 2015

Edited by S. Sasaki, Tokyo Institute of Technology, Yokohama, Japan

‡ Present address: Lortek, Arranomendi kalea 4A, 20240 Ordizia, Spain
§ Present address: Carl Zeiss Microscopy GmbH, Königsallee 9-21, 37081 Göttingen, Germany
¶ Present address: Leibniz-Institut für Kristallzüchtung, Berlin, Germany

Keywords: X-ray diffraction imaging; X-ray asterism; cracks; silicon; indentation.

Supporting information: this article has supporting information at journals.iucr.org/j

The asterism observed in white radiation X-ray diffraction images (topographs) of extended cracks in silicon is investigated and found to be associated with material that is close to breakout and surrounded by extensive cracking. It is a measure of the mechanical damage occurring when the fracture planes do not follow the low-index cleavage planes associated with the crystal structure. It is not related to a propensity for some cracked wafers to shatter during subsequent high-temperature processing. There is no correlation between crack morphology and alignment of an indenter with respect to the orientation of a silicon wafer, the cracks being generated from the apices of the indenter and having threefold symmetry for Berkovich indents and fourfold symmetry for Vickers indents. X-ray diffraction imaging (XRDI) of indents does not reveal this underlying symmetry and the images exhibit a very substantial degree of variation in their extent. This arises because the XRDI contrast is sensitive to the long-range strain field around the indent and breakout reduces the extent of this long-range strain field. Breakout is also detected in the loss of symmetry in the short-range strain field imaged by scanning micro-Raman spectroscopy. Weak fourfold symmetric features at the extremes of the images, and lying along ⟨110⟩ directions, are discussed in the context of slip generated below the room-temperature indents. Scanning electron microscopy imaging of the region around an indent during focused ion beam milling has permitted the three-dimensional reconstruction of the crack morphology. The surface-breaking Palmqvist cracks are found to be directly connected to the median subsurface cracks, and the presence of extensive lateral cracks is a prerequisite for material breakout at indenter loads above 200 mN. The overall crack shape agrees with that predicted from simulation.

1. Introduction

Although specific numbers are almost impossible to obtain owing to commercial confidentiality, it is widely accepted that catastrophic wafer breakage during high-temperature processing is a multi-million dollar problem in semiconductor manufacturing. Unlike previous approaches based on statistical analysis of fracture probability (Cook, 2006; Brun & Melkote, 2009; Chen *et al.*, 2009, 2010), we have developed an X-ray diffraction imaging (XRDI) technique for assessing the probability that individual cracks will propagate (Tanner *et al.*, 2012) during rapid thermal processing. This methodology now underpins commercial XRDI products which are available on the market.

Whereas a simple critical criterion, based on the ratio of the crack length to the width of the image at the crack tip in the X-ray topographs (Bowen & Tanner, 2006), satisfies the

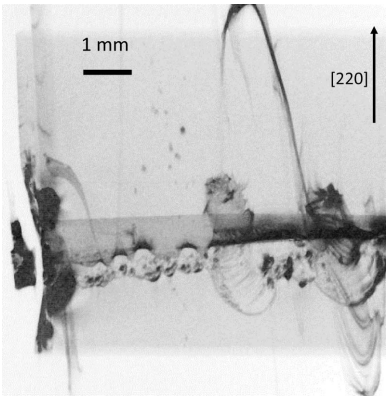

metrological requirements of the semiconductor industry, certain other features of the crack images are of interest to the crystallographer. In this article, we explore how the detailed examination of the X-ray diffraction contrast at cracks can provide further insight into the behaviour of cracks in brittle crystalline materials.

2. Experimental

X-ray diffraction imaging experiments were conducted on integrated-circuit-quality 200 mm (8 inch)-diameter dislocation-free silicon wafers, cut within 0.2° of the (100) orientation and purchased from Y Mart Inc., Palm Beach Gardens, Florida, USA. These double-side polished p-type wafers had resistivity below 10 Ω mm and were of thickness 725 (25) µm. Under optical inspection or in X-ray diffraction images, no edge defects were visible in the as-received wafers, which had been packed and shipped in standard cassettes. Indentation was used to create controlled amounts of damage at specific locations both close to and far away from the bevel edges. An Agilent Nanoindenter II tool equipped with a Berkovich tip was used for indentation loads up to 600 mN. A Mitutoyo AVK-C2 hardness tester equipped with a Vickers tip was used for application of heavier loads from 1 N up to 50 N (Garagorri *et al.*, 2010). All topographs shown in this article were taken in white beam at the ANKA synchrotron radiation facility of the Institute for Synchrotron Radiation, Karlsruhe Institute of Technology, Germany, or the Diamond Light Source, Didcot, Oxford, UK. At the TOPO-TOMO beamline of ANKA, transmission images were recorded on a CCD camera (Danilewsky *et al.*, 2011) optically coupled to a macroscope and with an $Lu_3Al_5O_{12}$ scintillator. The effective pixel size of the detection system was 2.5 × 2.5 µm. Back-reflection images were collected on high-resolution (Slavich VPR-M) X-ray film. At beamline B16 of the Diamond Light Source, transmission images were recorded with a CCD camera manufactured by PCO.Imaging GmbH, which has 4008 × 2672 pixels and a 14 bit dynamic range. Both sample and detector were mounted on the 2 × 1.2 m versatile optics table at the end of the beamline. Scintillators and objective lenses were chosen such that the pixel size was either 1 or 0.5 µm. In both cases, we binned adjacent pixels to give an effective resolution of 2 or 1 µm. Data acquisition times were between 10 and 40 s. All transmission diffraction images taken in the 022 reflection had a principal wavelength of 0.0506 nm. High-resolution reciprocal-space mapping was performed on a Bede D1 diffractometer and *ex situ* scanning electron microscopy (SEM) was performed on a field emission electron microscope (LEO 1525) with an in-lens secondary electron backscattering detector. A Quanta 3D dual beam FIB from FEI, which incorporates FEGSEM (field emission gun scanning electron microscopy) and FIB (focused ion beam) cannons, was used to make microscopic observations of cracks around indents as the specimen was FIB milled down. The electron and ion beam cannons form an angle of 52° to each other. The instrument incorporated SE (secondary electron), BS (backscattered electron) and STEM (scanning transmission electron microscopy) detectors. Micro-Raman strain mapping was performed with a Jobin-Yvon HORIBA HR800 system running *LabSpec 5* software. The system is integrated with a microscope coupled confocally to an 800 mm-focal-length spectrometer. The samples were mounted on a high-precision table capable of *x*–*y* and *z* translation. The table can be moved manually and is also motorized and can be controlled either by a joystick or directly from the *LabSpec* software. A diffraction grating of 1800 groves per millimetre was used to split the Raman signal into individual wavelengths, which are then directed onto a CCD detector. Using an Ar+ 488 nm laser the penetration depth of the light into the sample was about 565 nm.

Three-dimensional reconstruction of the cracks was done from the FIB cross section using *Amira* software reconstruction. Simulation of the crack geometry was performed using the commercial software *ABAQUS* (version 6.8-3). The code incorporates a cohesive zone model (Dugdale, 1960; Barenblatt, 1962; Tvergaard & Hutchinson, 1992; Chowdhury & Narasimhan, 2000; Turon *et al.*, 2007) which assumes that a cohesive damage zone develops near the crack tip and thereby links the microstructural failure mechanisms to the continuum field governing the bulk deformations. Damage initiation is related to the peak stress, there being several types of constituent equation used to relate cohesive elements. We have used a simple triangular relation between stress and crack face separation (Gorostegui-Colinas, 2012).

3. Results

3.1. Asterism from crack images

At a load of 50 N, with a Vickers tip, indentations close to the bevel edge generated millimetre-length cracks (Tanner *et al.*, 2012) which sometimes resulted in catastrophic wafer breakage during rapid thermal annealing. As we have shown in the above reference, the cracks which are the most dangerous and likely to cause catastrophic wafer breakage during high-temperature processing are those whose X-ray diffraction images are sharp, and where the ratio κ of the crack length to the width of the crack tip image is high. A crack

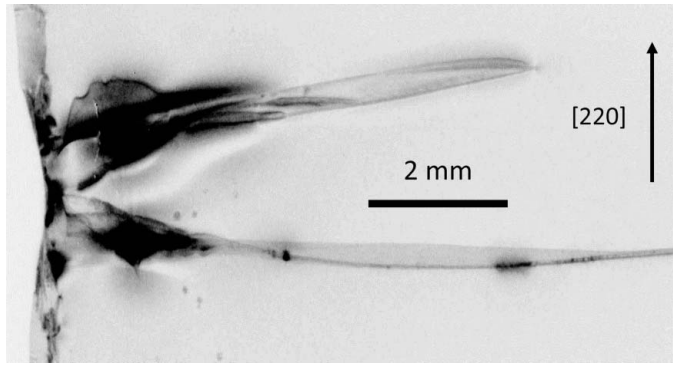

Figure 1
X-ray diffraction image of a pair of dangerous cracks, exhibiting a high length to crack tip image width ratio. X-ray wavelength 0.0506 nm.

which exhibits a large image width at its tip is likely to be benign, whereas cracks such as those shown in Fig. 1 are highly dangerous to wafer integrity. The critical value κ_c between dangerous and benign cracks depends on the geometry and thermal gradients of the processing furnace. In the example shown, the cracks were initiated by an indent at the bevel edge at the left of the 200 mm-diameter wafer and neither crack lies on a low-index crystallographic plane. Nevertheless, the crack images are simple and localized and the features principally correspond to direct kinematical images (μt = 0.6 at λ = 0.0506 nm).

However, many of the crack images, whether or not the cracks lie on low-index planes, exhibit substantial asterism in the white radiation diffraction topographs (Fig. 2). Both high- and low-κ value cracks may exhibit asterism. Such asterism was found not to be solely a feature of cracks but was also found in images from the broken edges of wafers after cracks had propagated. Asterism in white radiation topographs is a form of 'orientation contrast' (Bowen & Tanner, 1998) and arises from the displacement in space of X-ray-diffracted intensity owing to a large effective misorientation of the crystal lattice around a defect. Tilt $\delta\theta$ and dilation δd of Bragg planes of spacing d combine such that there is an effective misorientation $\Delta\theta$, given by

$$\Delta\theta = (\delta d/d)\tan\theta_B \pm \delta\theta, \qquad (1)$$

where θ_B is the Bragg angle. In the synchrotron white beam experiment, the incident beam is highly parallel but has a wide range of wavelengths present. Misoriented regions therefore select the appropriate wavelength for diffraction, the effective misorientation of the diffracted beam being $2\Delta\theta$. This may be determined straightforwardly by measuring the extent of the asterism, in a direction parallel to the diffraction vector, as a function of displacement of the detector from the sample.

In the small-angle limit, the asterism extent is found to vary linearly with displacement for a number of examples (A–D in Fig. 3), the gradient increasing with increasing X-ray wavelength.

The tilt $\delta\theta$ and strain $\delta d/d$ can be separated by measuring the variation of asterism extent *versus* detector displacement as a function of the X-ray wavelength. Although the range of Bragg angles available is limited at longer wavelengths by absorption resulting in a complicated image and at short wavelengths by the need to separate incident and diffracted beams, the trend is clear for all features. Two examples are illustrated in Fig. 4. For the two asterism features the associated tilt was found to be 0.216 (6) and 0.222 (5)°, while the corresponding strain was 0.0061 (8)–0.0050 (9).

The tilt and strains measured above are large compared with those across the tight cracks. That measurement can be made in a standard high-resolution X-ray diffractometer by locating a beam of typically 1 mm diameter over both sides of the crack and recording a reciprocal-space map. An example is shown in Fig. 5. It is immediately apparent that the dominant feature is an abrupt tilt across the crack, as what is normally a single peak is split into two in the q_x direction. Dilations affect the scattering in the q_z direction, and as there is neither displacement nor broadening of the peaks in this direction, one may conclude that across cracks such as illustrated in Fig. 1 there is little strain. The two sides of the crack are simply misoriented with respect to each other. However, the displacement is measured to be small, in this case 0.025 (1)°, and an order of magnitude less than that associated with the asterism described above.

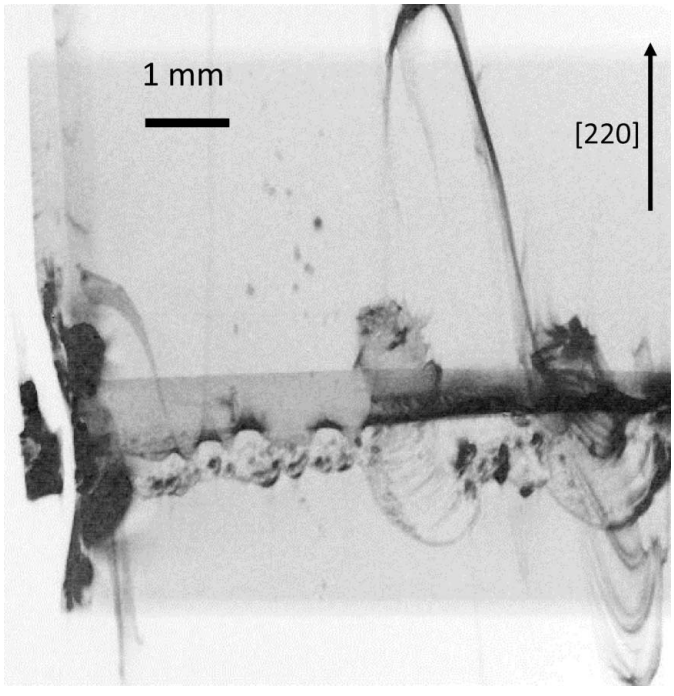

Figure 2
Part of a crack image showing extremely strong asterism. Indent at left of image. Transmission X-ray diffraction image with specimen-to-detector distance 138 mm.

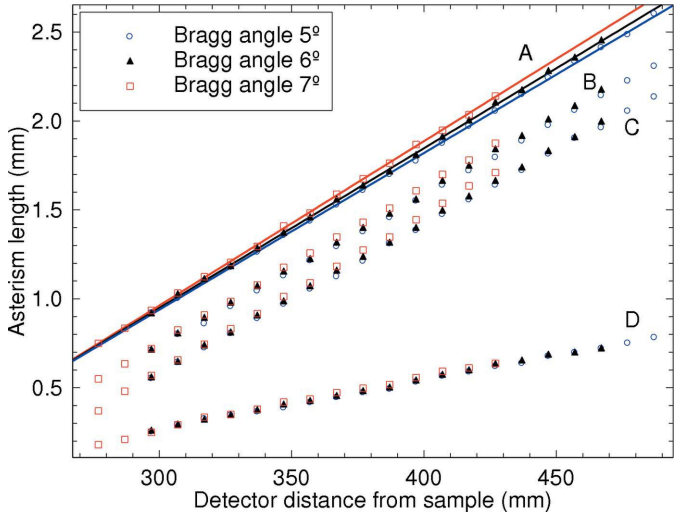

Figure 3
Extent of the asterism streak, measured in the direction of the diffraction vector, in four separate features (A, B, C and D) as a function of displacement of the detector with respect to the specimen, measured at three different X-ray wavelengths. The solid lines are least-squares fits of data to a linear function.

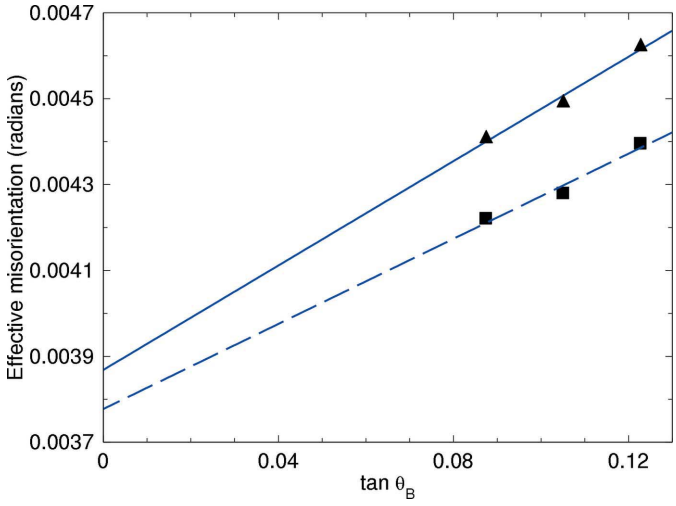

Figure 4
Effective misorientation as a function of Bragg angle for two individual asterism features. The intercept gives the tilt, the gradient gives the strain.

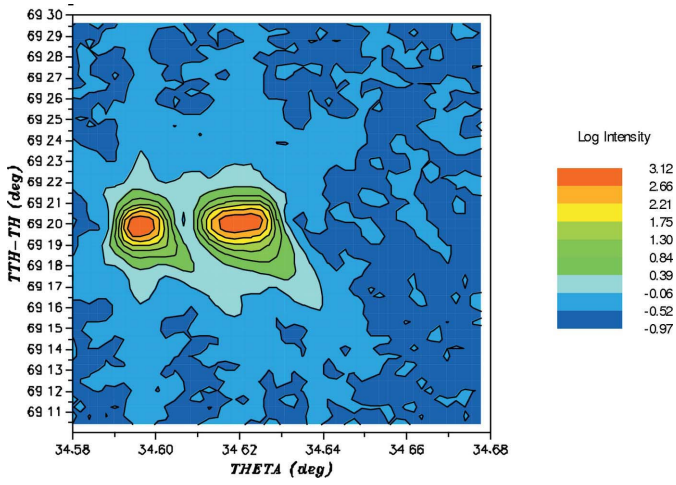

Figure 5
Reciprocal-space map recorded with the X-ray beam covering both sides of a tight crack, generated by indentation close to the bevel edge of the wafer. Cu $K\alpha_1$ radiation, surface symmetric 400 reflection.

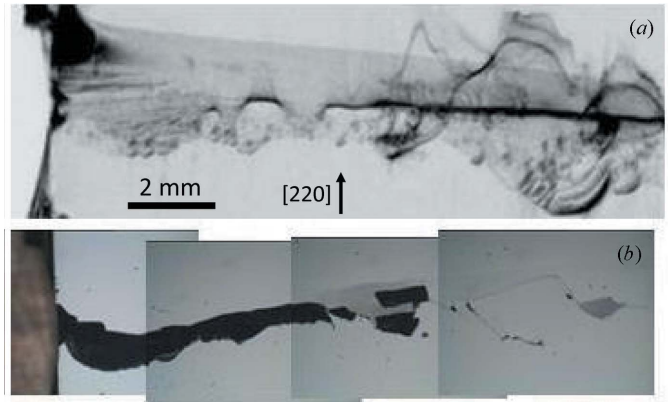

Figure 6
(*a*) Transmission X-ray diffraction image (topograph) of a crack showing significant asterism compared with (*b*) an optical image of the same area. Strong asterism arises in the region where there is substantial crack branching but no breakout of material. Specimen-to-X-ray-detector distance 138 mm.

A systematic survey of the cracks using optical microscopy has revealed that, in all cases where asterism has occurred, the crack has branched and deviated from a simple path. In many cases, breakout of material has been found in the vicinity of the asterism features. An example of the association, typical of many, is shown in the X-ray topograph (Fig. 6*a*) and the corresponding optical micrograph of the area (Fig. 6*b*). The strongest asterism is seen on the right of the image, which corresponds to the region where breakout has not occurred, but where the crack has branched. From the shape of the cracks it appears likely that breakout has nearly occurred and that further stress on the crack would result in material being broken off. Though not fully broken out, the material bordered by the two branches of the crack will be tilted and strained with respect to the main wafer, resulting in the observed asterism.

3.2. Indents and their crack morphology

When indentation takes place away from the wafer edge, the crack system is found to be much more localized and millimetre-length cracks are not observed, even at the highest indenter loads (up to 50 N). The X-ray diffraction images of indents give almost no information concerning the location or orientation of the micro-cracks generated by room-temperature indents in silicon. In the back-reflection (Bragg) geometry the diffracted image is sensitive to strains near to the surface, not throughout the wafer. Many of the images recorded in a single exposure of a (001) silicon wafer oriented perpendicular to the incident beam correspond to high-index reflections where, because of the high scattering vector, the value of the scattering factor is low. As a result, there is high strain sensitivity.

White radiation back-reflection indent images are characterized by a central region with very substantial loss of diffracted intensity, surrounded by a ring of enhanced intensity and weak diffuse images of enhanced intensity outside of this ring. An excellent example is shown in Fig. 7, which corresponds to a 0 2 10 reflection with a Bragg angle of 88.69° and corresponding wavelength of 1.06 Å selected by the wafer. The images are of five rows of Berkovich indents at 100, 200, 300, 400 and 500 mN and one row of Vickers indents at 2 N load. In this, and all other images on the film, there are no features corresponding to the symmetry of the indenting tip, which is threefold for the Berkovich tip and fourfold for the Vickers tip. This is despite very clear evidence in two-dimensional micro-Raman scans of a threefold symmetry in the strain field around low-load Berkovich indents (Fig. 8*a*). The experimental evidence is supported by finite element calculations of the stress fields (Fig. 8*b*), which also show threefold symmetry. However, these data come from regions typically a few micrometres across and within the footprint of the indenter tip. Because of the higher strain sensitivity of X-ray topography compared with Raman scattering, the X-ray images extend over a diameter an order of magnitude larger than that of the region probed by micro-Raman spectroscopy and no information from the latter can be extracted from the

X-ray scattering. (We note that typically quoted stress sensitivities for Raman spectroscopy of Si are of the order of 20–50 MPa. This implies strain sensitivity of the order of 0.1–0.3%, *i.e.* parts in 10^4. A typical X-ray Darwin width is 5″, giving a strain sensitivity of parts in 10^5.)

The loss of intensity in the centre of the X-ray image must correspond to orientation contrast, *i.e.* the strained region around the indent is so highly misoriented that either no X-rays of suitable wavelength for diffraction are present in the white beam or, because of the different wavelength selected, the directions of the diffracted beams differ substantially from that of the perfect crystal. The high-intensity ring surrounding the area of intensity loss corresponds to the piling up of the deflected X-ray intensity.

The symmetry of cracks generated at the apices of the indenter tips reflects the tip geometry (Fig. 9). However, we note that the extent of the cracks in the SEM images is much lower than the extent of the X-ray image. For example, in the case of the 200 mN Berkovich indent, the cracks extend up to 5 µm from the centre of the indent, whereas the radius of the circular X-ray image is about 35 µm. Similarly, for the 2 N Vickers tip, the cracks extend 25 µm whereas the X-ray image is 100 µm in radius. There is, however, no variation in the crack geometry as a function of crystallographic direction with respect to the ⟨110⟩ directions in the plane of the wafer. Cracks emerge from the location of the indenter apices.

A feature which is not related to the symmetry of the indenter or the cracks generated is the presence of the short radial lines seen at the periphery of the enlarged images in Fig. 7(*b*). The radial lines run in the ⟨110⟩ directions and thus are not related to the symmetry of the cracks at the Berkovich tip apices. Such lines are found in ⟨110⟩ directions in most reflections, although in some images, not all lines appear and the fourfold symmetry is absent. They are not simply related geometrically to the diffraction vector projection direction. A possible explanation of these features might be that they are orientation contrast associated with dislocations generated below the indents. Slip is on {111}⟨110⟩ systems and slip bands project into the two ⟨110⟩ directions in the wafer plane. Whereas silicon is brittle at room temperature, we note that the dislocation velocity $\upsilon(\tau, T)$ under an imposed stress field τ varies as

$$\upsilon(\tau, T) = A(\tau/\tau_0)^{m(T)} \exp[-E/(k_B T)], \qquad (2)$$

where E is the activation energy, A and τ_0 are constants, k_B is the Boltzmann constant, and m is close to unity and a function

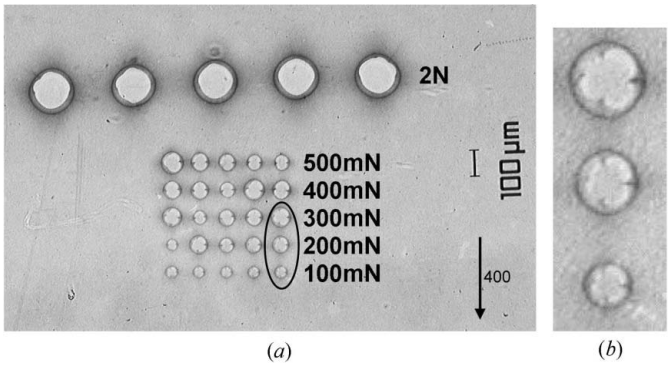

Figure 7
White radiation topography images of indents taken in the Bragg (reflection) geometry. The 0 2 10 reflection corresponding to a wavelength of 1.06 Å. The enlargement (*b*) of the encircled area shows fourfold symmetric radial images from threefold symmetric Berkovich indents. The specimen-to-detector distance was 85 mm.

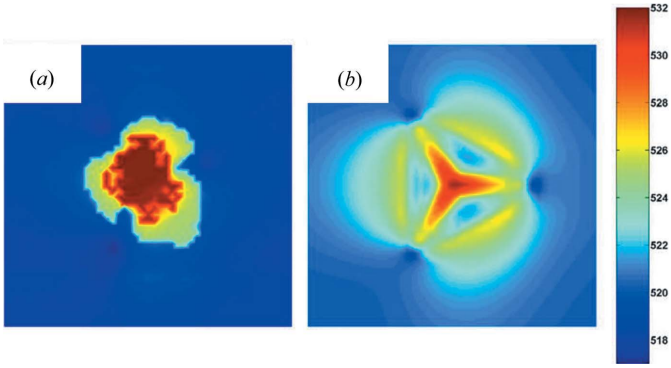

Figure 8
(*a*) Experimental two-dimensional Raman map and (*b*) finite element simulation of the stress field for a 150 mN Berkovich indent.

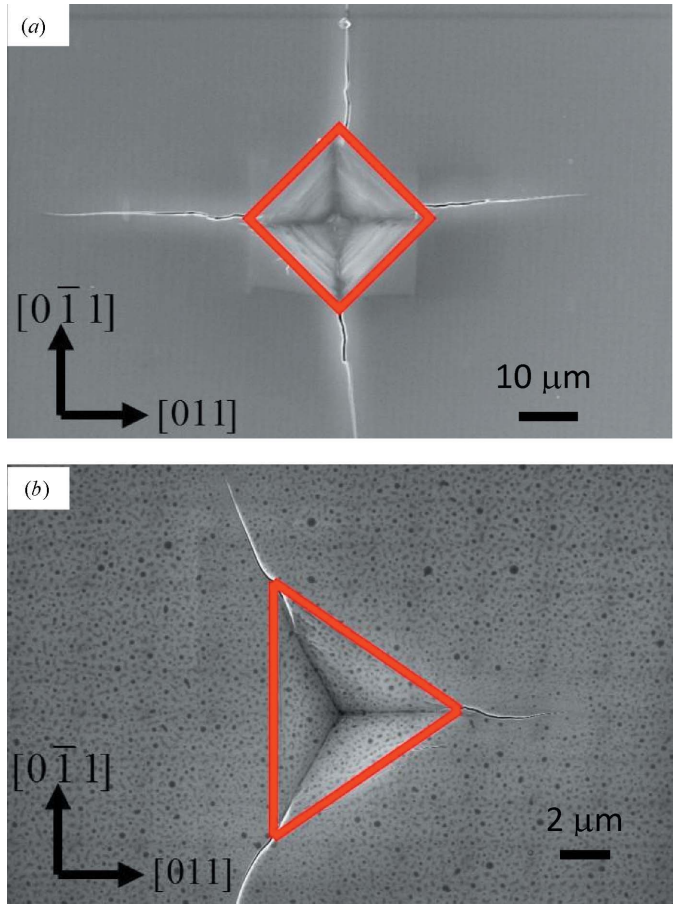

Figure 9
Scanning electron microscope images of cracks generated from (*a*) a 2 N load on a Vickers tip and (*b*) a 200 mN load on a Berkovich tip. Superposed red lines indicate the footprint of the indenter tips.

of temperature T. The activation barrier is reduced by the imposed stress, with a result that the velocity under the tip changes from almost zero at room temperature to a significant value under stress. Slip dislocations have been observed beneath indents made at room temperature (Saka *et al.*, 2002; Minor *et al.*, 2005), and STEM analysis of the region below our indents (Fig. 10) shows similar dislocation networks to those previously reported (Brady *et al.*, 2000). Whereas there is no evidence in Fig. 10 of other phases in the STEM image, down to 150 mN, the load displacement curves during indentation show the pop-in and pop-out phenomena which are attributed *via* micro-Raman spectroscopy analysis to the transformation from the Si-I to the Si-III and Si-XII phases (Allen *et al.*, 2010).

The dislocations emerge from the tip of the median crack running from the bottom left of the image. Similar blunting of the crack tip by dislocation emission was observed in our *in situ* XRDI experiments of the movement of cracks subjected to temperature gradients (Danilewsky *et al.*, 2013). The high density of dislocations in the region marked with a rectangle may indicate that the lateral crack was arrested before changing direction and propagating almost parallel to the surface under the indenter.

Although we have not been able to establish the complete geometrical arrangement of these defects, we can establish that the observed dislocations lie in ⟨110⟩ directions on the inclined {111} slip planes which have the fourfold symmetry within the (001) plane, which is characteristic of the X-ray image contrast. However, in agreement with previous observations, we note that the dislocations do not extend more than about a micrometre from the indent, and bearing in mind the absence of evidence for the crack geometry in the X-ray image, it is not clear how these dislocation slip bands can give rise to long-range contrast, if indeed they do so.

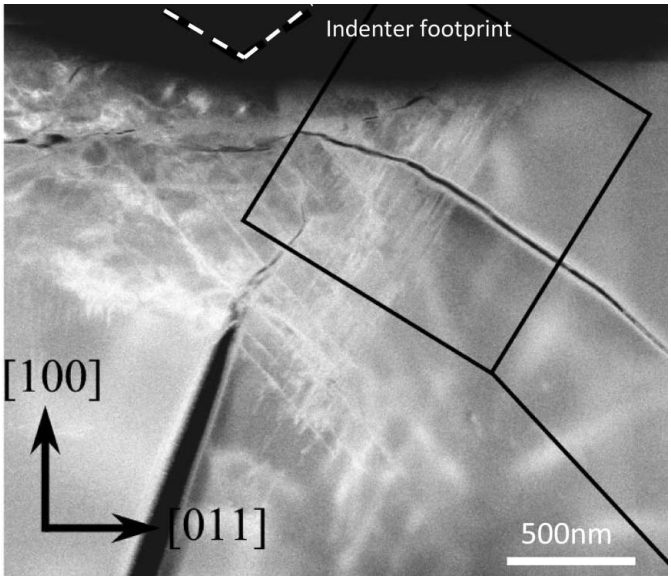

Figure 10
Dislocation array below a 150 mN Berkovich indent observed by STEM.

3.3. Dispersion of crack lengths and X-ray image size

Measurement of the total crack length observed in the SEM images of Berkovich indents revealed a simple linear relationship between indenter load and crack length (Fig. 11). The large error bars associated with the data points do not arise from imprecision in measurement but rather from the dispersion in the length of individual cracks. As might be expected for a stochastic process such as crack propagation, repeated indentation does not result in identical crack length. However, what is noteworthy is that the dispersion rises markedly with indenter load, the 1σ error bar rising from 35% at 100 mN to 75% at 500 mN.

Similar dispersion is observed in the size of the indentation images in the X-ray topographs. This can be seen both in the back-reflection images of Fig. 7 and in the transmission images of Fig. 12. There, the extent of the image in the diffracted beam direction varies from 139 to 96 µm.

We have noted that, above about 200 mN load, breakout of material is observed around the indent, whereas below this

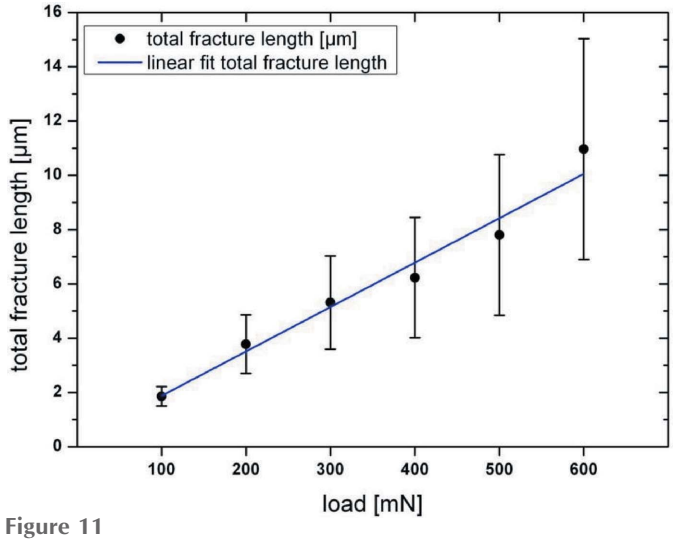

Figure 11
Total crack length as a function of indenter load.

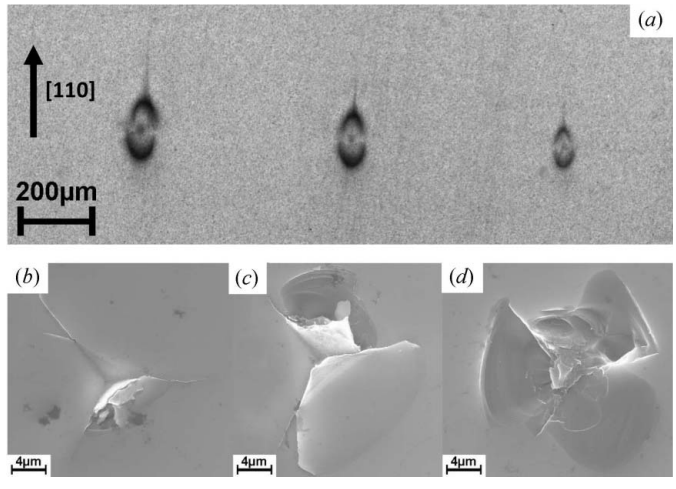

Figure 12
(*a*) Transmission X-ray diffraction images (220 reflection), and SEM images (*b*)–(*d*), of the same three 600 mN indents.

load, breakout does not occur. In §3.1, we noted that the presence of asterism was associated with material that was tilted but not completely broken away. The SEM images in Fig. 12 reveal that when full breakout does occur, as in the right-hand image, the X-ray image is reduced in spatial extent. We have many examples of this correlation between complete breakout and the reduction in the strain field revealed in the X-ray topographs.

3.4. Subsurface crack geometry and breakout

In a recent review, Lawn & Cook (2012) described the crack systems associated with indentation of brittle materials. The surface breaking radial cracks at the apices of the indents, such as illustrated in Fig. 9, are the so-called Palmqvist cracks and are found in a range of brittle materials. Tancret (2000) reported evidence that they are the first type of crack to form during loading, reaching their maximum extent during unloading. Lawn & Cook (2012) have argued that radial and median cracks below the indenter are all part of the same crack system. Our SEM images of the crack distribution as a function of depth of material removed by FIB milling definitely support this latter attribution (Fig. 13). There is a continuous elongation of the Palmqvist cracks as a function of depth (Figs. 13*b* and 13*c*), and they eventually merge into the subsurface median cracks which join at the base of the indenter (Fig. 13*d*).

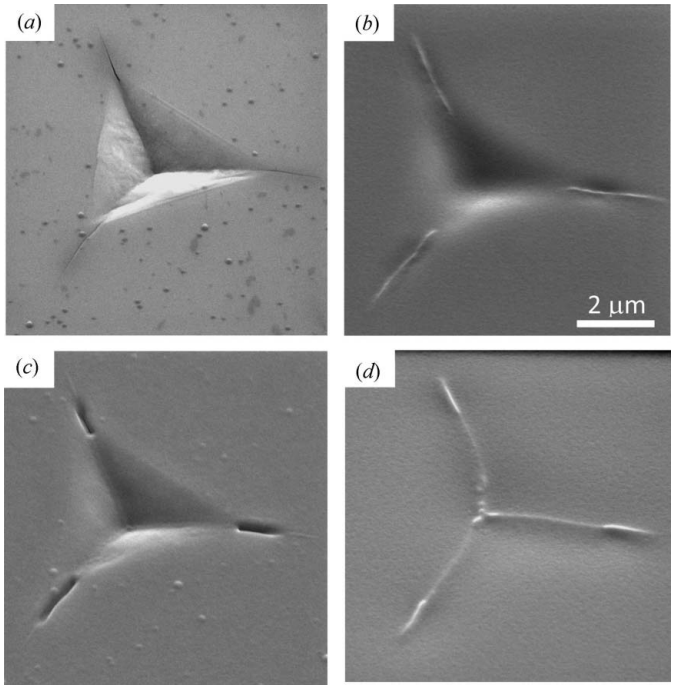

Figure 13
SEM images of cracks on the wafer surface during removal of material by focused ion beam milling following a 110 mN Berkovich indentation. (*a*) Palmqvist cracks associated with the tip apices prior to removal of material. (*b*) Opening of cracks due to strain relief from milling. (*c*) Extension of crack length breaking the surface. (*d*) Merging of Palmqvist cracks with the median cracks formed below the indenter tip itself.

The shape of the median cracks can be revealed by a three-dimensional reconstruction of the crack from images taken as a function of time during FIB milling. Using the top-milling technique illustrated in Fig. 13, it proved to be difficult to measure the depth of the material removed with the accuracy needed for a good three-dimensional reconstruction. Images for reconstruction were thus taken in cross section. These show similar structures at the three apices of the indent depression. Fig. 14 shows an example of one such median crack associated with one apex of the indenter. It lies, at least approximately, on a plane containing the [001] normal to the wafer surface. There is no distinction between the subsurface and the surface-breaking (Palmqvist) region of the crack. The length measured from the crack reconstruction at the sample surface, identified in the image by the dashed lines, correlates quite well with the average length plotted in Fig. 11 for a 120 mN Berkovich indent.

At higher indenter loads, the crack geometry becomes much more complex with substantial lateral cracks emerging by 140 mN, and by 200 mN loads, the lateral cracks extend beyond the median and Palmqvist cracks. Further, at the higher loads, the median cracks are no longer perpendicular to the wafer surface. In one case, a deviation of 28° was observed. At 500 mN load, the lateral cracks are very extensive (Fig. 15*a*), and although starting from typically a micrometre below the indenter, they tend to turn upwards as they extend. Viewed from along the [001] direction (Fig. 15*b*) one may observe that the lateral crack is limited in area by its intersection with the median cracks, which emerge from the indent apexes and run horizontally and vertically in the image. This results in a shape characteristic of the material which breaks out around the indent. Although this particular crack did not intersect the surface, it is evident that further propagation would have resulted in the formation of the characteristically shaped breakout chips illustrated in Fig. 12. The presence of extensive lateral cracks seems to be a prerequisite for breakout to occur.

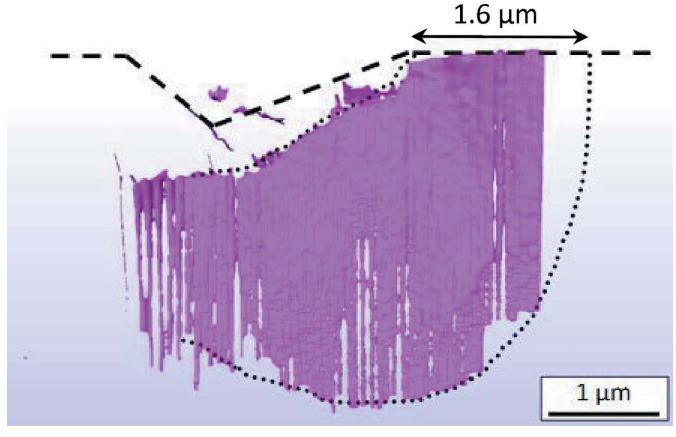

Figure 14
Median/Palmqvist crack below the impress of a 120 mN Berkovich indenter. The image is reconstructed from a series of cross section images from trenches milled across the indents. The dashed lines indicate the surface of the sample and the Berkovich indent profile, and the dotted lines delimit the median/Palmqvist crack.

Fig. 15(*c*) is a FEGSEM micrograph of the same Vickers indent before cross section milling. The area marked A corresponds to the sector specifically selected for crack reconstruction, where no breakout is observed. In contrast, sectors B and C do reveal two severe breakouts. The relation between breakout and increasing indentation load is revealed in this case as the lattice tries to release the strain energy in the form of lateral cracks; some of them reach the surface, others do not. Eventually, when the load from indentation is high enough (of the order of a few newtons in our studies), lateral cracking will result in complete breakout at the four edges of the Vickers indent.

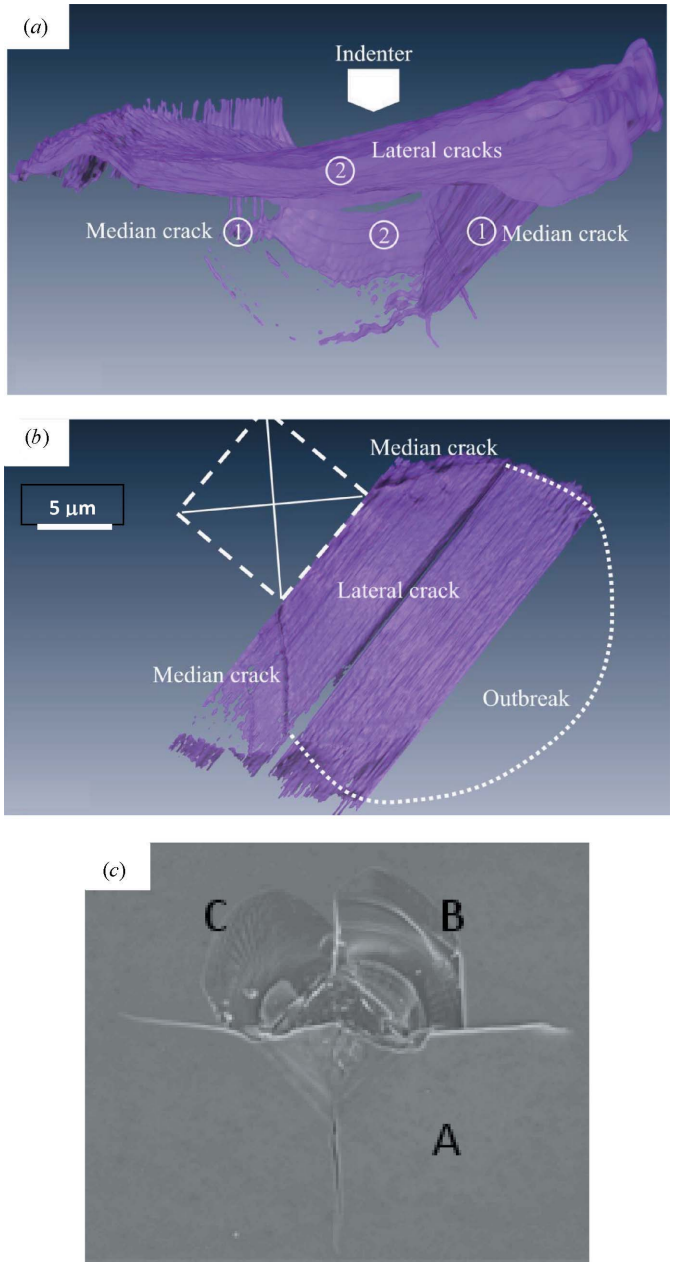

Figure 15
Reconstruction of cracks observed below a 500 mN Vickers indent: from (*a*) a direction parallel to the side of the Vickers indent and (*b*) the [001] direction. The diamond (dashed lines) depicts the Vickers imprint, and the dotted lines approximately delimit the virtual breakout, if the lateral crack had emerged at the sample surface. (*c*) FEGSEM micrograph of the indent before cross section milling.

4. Discussion

The above observations indicate that the presence of asterism in X-ray diffraction topographs of cracks in a brittle material is associated with tilted and elastically strained material that is close to breakout. Whereas asterism is primarily associated with regions where the crack has deviated from a low-index plane, often branching prior to the initiation of material breakout, examples of limited asterism have been found when the crack is straight and lying on a (111) plane. In these cases, the regions giving rise to the asterism are of limited extent and usually close to places where some material breakout has occurred. The presence of asterism does not appear to be related to the width of the crack tip in the X-ray diffraction images or the κ value and hence it does not give an indication of the propensity of the crack to result in catastrophic failure during subsequent high-temperature thermal processing.

The X-ray diffraction images of the micro-cracks introduced by nanoindentation do not reveal the symmetry of the median cracks, which is determined by the indenter tip shape, not by the orientation with respect to the wafer crystallographic coordinates. Indeed, the crystal symmetry does not appear to affect the crack symmetry.

The dispersion in the X-ray images of indentations, a graphical example of which is given in Fig. 16, does depend on whether breakout occurs. In Fig. 16, as in other examples, there seem to be two families of data points (triangles and squares in the plot) corresponding to the case where breakout does and does not occur. While there is no difference in the indentation process between these two sets, the triangular points lie systematically below the squares, the latter having a smaller distribution of values. Straight lines of almost equal gradient can be fitted to the two data sets, the squares corre-

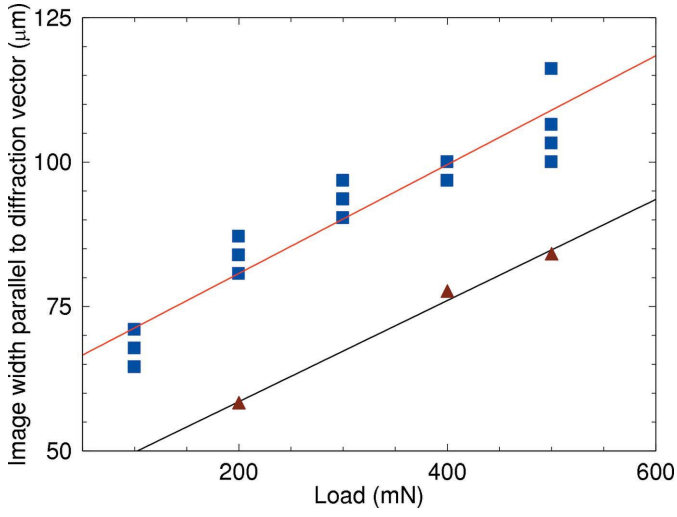

Figure 16
Width of the contrast feature, parallel to the diffraction vector, of X-ray diffraction images taken in transmission of Berkovich indentations of differing loads (see Fig. 12).

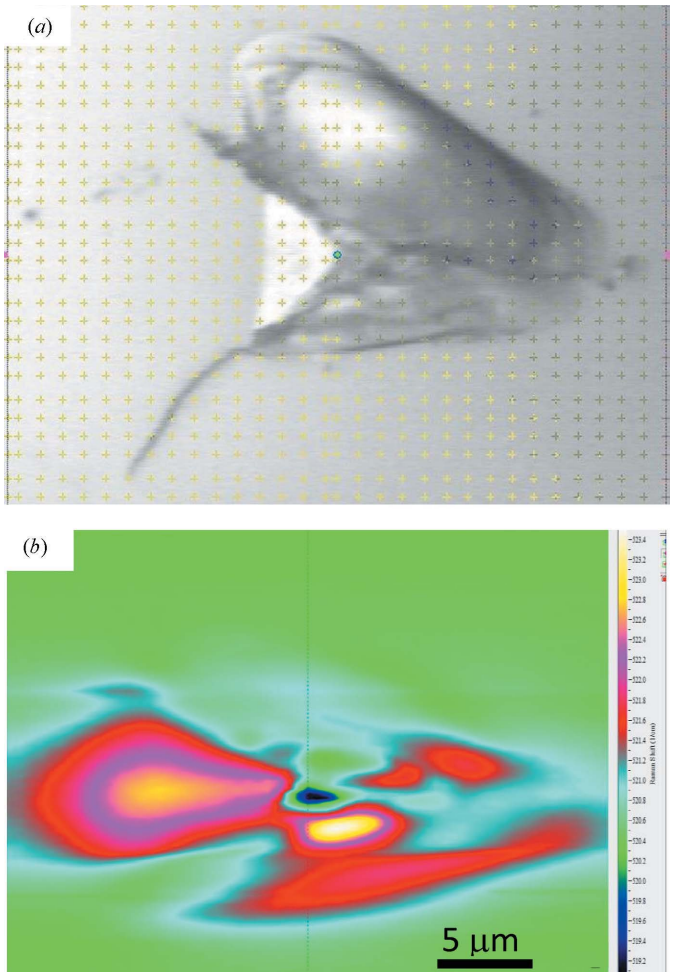

Figure 17
(*a*) Optical image of a 600 mN load Berkovich indentation, showing substantial breakout occurring in the upper right-hand sector of the indent damage. (*b*) Two-dimensional micro-Raman map of strain around the indentation; the pseudo-colour scale corresponds to the Raman peak shift in the spectra from individual points.

sponding to indents where material had not broken out, and the triangles corresponding to indents where significant breakout had occurred. Although the X-ray images accurately record the amount of residual strain present, one cannot reverse the analysis and deduce the indenter (or misaligned handling tool) load that had been applied to the wafer. Nevertheless, by examining statistically the maximum extent of the edge damage associated with handling tools, some indication of the tool alignment can be obtained.

Whereas breakout of material from one sector of the indenter damage does not result in asymmetry in the X-ray image, the resulting symmetry breaking can be detected in techniques with a higher spatial (but lower strain) resolution such as micro-Raman spectroscopic imaging. Fig. 17(*a*) shows an optical image of an indent where breakout has occurred in the upper right-hand side of the damaged region. In the corresponding two dimensional micro-Raman strain map built up from multiple point-by-point spectral scans (Fig. 17*b*), the loss of material through the breakout shows up as a loss of residual strain. The Raman shift is linearly reduced by tensile strain and increased by compressive strain. We found the strain at some distance away from the indenter tip to be compressive and of the order of 0.5 GPa, while directly beneath the indent, the strain was tensile and about 3.2 GPa. This is consistent with the presence of a voided region, such as a crack, beneath the indent which could produce a surrounding tensile strain field (Lawn & Evans, 1977; Lawn, 2004).

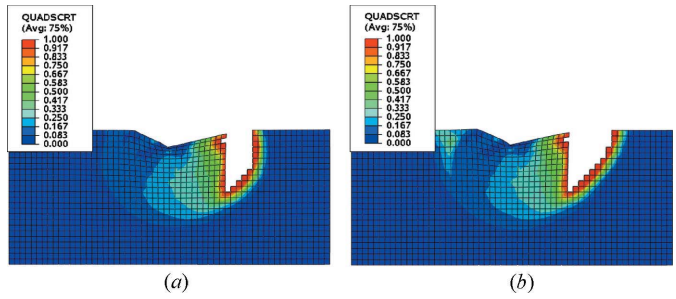

Figure 18
Simulation of the formation of a median crack associated with a 75 mN Berkovich indentation: (*a*) during loading and (*b*) following unloading.

The crack morphology revealed by the reconstruction from the SEM images taken during FIB milling of the indent is consistent with analysis of the micro-Raman maps. Above 120 mN (Fig. 14) the median cracks extend to the region directly below the indenter tip. Simulation of the cracking process suggests that the propagation of the median cracks into this region takes place during the unloading process.

Fig. 18 shows a simulation of the median crack formation for a 75 mN Berkovich indent. We note that the general shape of the stress field, as well as the shape of the outer edge of the crack itself, agrees well with the experimentally observed crack shapes (Fig. 14). The extent and location of the simulated crack depends on the fracture energy introduced into the *ABAQUS* code. However, owing to the statistical nature of the fracture process, there are a range of lengths measured experimentally (Figs. 11 and 12), and use of fracture energies between 3.84 and 3.5 J m^{-2} results in simulated lengths lying within the experimental range. Specifically the former gives a crack of length 1.4 µm and the latter a length of 1.6 µm. These both compare well with an experimental length of 1.5 (4) µm extrapolated to 75 mN from the data in Fig. 11.

5. Conclusions

We conclude from the studies described above that the presence of asterism in X-ray diffraction images of cracks in silicon is associated with material that is near to breakout. Owing to the presence of lateral cracks, thin segments of material are tilted and strained in such a way that the effective misorientation becomes large, resulting in displacement of the diffracted beams in space and giving rise to orientation contrast in white radiation topographs. X-ray diffraction images of indents do not reveal the crack geometry or symmetry. Breakout of material is responsible for the substantial variation in the extent of the X-ray images, and the

loss of symmetry associated with breakout is observed in the shorter-range strain fields imaged by scanning micro-Raman spectroscopy. The presence of asterism does not appear to be connected in any way with the probability that a wafer containing a crack will shatter on subsequent high-temperature thermal processing. Asterism can be observed whether or not a crack lies on a low-index plane and when the crack tip in the X-ray diffraction images is either wide or narrow.

Acknowledgements

Financial support was provided through the European Community FP7 STREP project SIDAM (grant No. FP7-ICT-216382). Technical support from Kawal Sawhney and Igor Dolbnya at beamline B16 of the Diamond Light Source and P. Vagovic, T. dos Santos Rolo and H. Schade at ANKA (Angströmquelle Karlsruhe) is gratefully acknowledged. Thanks are extended to other SIDAM consortium members, particularly Keith Bowen, for valuable discussion and Matteo Fossati for help in data collection.

References

Allen, D., Wittge, J., Zlotos, A., Gorostegui-Colinas, E., Garagorri, J., McNally, P. J., Danilewsky, A. N. & Elizalde, M. R. (2010). *Nucl. Instrum. Methods Phys. Res. Sect. B*, **268**, 383–387.
Barenblatt, G. (1962). *Adv. Appl. Mech.* **7**, 55–129.
Bowen, D. K. & Tanner, B. K. (1998). *High-Resolution X-ray Diffractometry and Topography*. London: Taylor and Francis.
Bowen, D. K. & Tanner, B. K. (2006). *X-ray Metrology in Semiconductor Wafer Manufacture*. Boca Raton: CRC Press, Taylor and Francis.
Bradby, J. E., Williams, J. S., Wong-Leung, J., Swain, M. V. & Munroe, P. (2000). *Appl. Phys. Lett.* **77**, 3749–3751.
Brun, X. F. & Melkote, S. N. (2009). *Sol. Energy Mater. Sol. Cells*, **93**, 1238–1247.
Chen, P. Y., Tsai, M. H., Yeh, W. K., Jing, M. H. & Chang, Y. (2009). *Jpn. J. Appl. Phys.* **48**, 126503.
Chen, P. Y., Tsai, M. H., Yeh, W. K., Jing, M. H. & Chang, Y. (2010). *Microelectron. Eng.* **87**, 2065–2070.
Chowdhury, R. S. & Narasimhan, S. R. (2000). *Acad. Proc. Eng. Sci.* **25**, 561–587.
Cook, R. F. (2006). *J. Mater. Sci.* **41**, 841–872.
Danilewsky, A. N., Wittge, J., Hess, A., Cröll, A., Rack, A., Allen, D., McNally, P. J., dos Santos Rolo, T., Vagovič, P., Baumbach, T., Garagorri, J., Elizalde, M. R. & Tanner, B. K. (2011). *Phys. Status Solidi A*, **208**, 2499–2504.
Danilewsky, A., Wittge, J., Kiefl, K., Allen, D., McNally, P., Garagorri, J., Elizalde, M. R., Baumbach, T. & Tanner, B. K. (2013). *J. Appl. Cryst.* **46**, 849–855.
Dugdale, D. S. (1960). *J. Mech. Phys. Solids*, **8**, 100–104.
Garagorri, J., Gorostegui-Colinas, E., Elizalde, M. R., Allen, D. & McNally, P. (2010). *An. Mec. Fract.* **27**, 559–565.
Gorostegui-Colinas, E. (2012). PhD thesis, Universidad de Navarra, San Sebastian, Spain.
Lawn, B. R. (2004). *J. Mater. Res.* **19**, 22–29.
Lawn, B. R. & Cook, R. F. (2012). *J. Mater. Sci.* **47**, 1–22.
Lawn, B. R. & Evans, A. G. (1977). *J. Mater. Sci.* **12**, 2195–2199.
Minor, A. M., Lilleodden, E. T., Jin, M., Stach, E. A., Chrzan, D. C. & Morris, J. W. Jr (2005). *Philos. Mag.* **85**, 323–330.
Saka, H., Shimatani, A., Sunaguma, M. & Suprijadi (2002). *Philos. Mag. A*, **82**, 1971–1981.
Tancret, F. (2000). *Scr. Mater.* **43**, 9–14.
Tanner, B. K., Fossati, M. C., Garagorri, J., Elizalde, M. R., Allen, D., McNally, P. J., Jacques, D., Wittge, J. & Danilewsky, A. N. (2012). *Appl. Phys. Lett.* **101**, 041903.
Turon, A., Davila, C., Camanho, P. & Costa, J. (2007). *Eng. Fract. Mech.* **74**, 1665–1682.
Tvergaard, V. & Hutchinson, J. W. (1992). *J. Mech. Phys. Solids*, **40**, 1377–1397.